PAPER • OPEN ACCESS

Finite-time quantum Stirling heat engine

To cite this article: S Hamedani Raja *et al* 2021 *New J. Phys.* **23** 033034

View the article online for updates and enhancements.

New Journal of Physics

The open access journal at the forefront of physics

PAPER

Finite-time quantum Stirling heat engine

S Hamedani Raja[1,2,*] ⓘ, S Maniscalco[1,2,3], G S Paraoanu[2] ⓘ, J P Pekola[2] and N Lo Gullo[1] ⓘ

1   QTF Centre of Excellence, Turku Centre for Quantum Physics, Department of Physics and Astronomy, University of Turku, 20014 Turku, Finland
2   QTF Centre of Excellence, Department of Applied Physics, Aalto University, FI-00076 Aalto, Finland
3   QTF Centre of Excellence, Department of Physics, PO Box 43, FI-00014, University of Helsinki, Finland
*   Author to whom any correspondence should be addressed.

E-mail: sina.hamedaniraja@aalto.fi

Abstract

We study the thermodynamic performance of a finite-time non-regenerative quantum Stirling-like cycle used as a heat engine. We consider specifically the case in which the working substance (WS) is a two-level system (TLS). The Stirling cycle is made of two isochoric transformations separated by a compression and an expansion stroke during which the WS is in contact with a thermal reservoir. To describe these two strokes we derive a non-Markovian master equation which allows to study the real-time dynamics of a driven open quantum system with arbitrary fast driving. Following the real-time dynamics of the WS using this master equation, the endpoints of the isotherms can deviate from the equilibrium thermal states. The role of this deviation in the performance of the heat engine is addressed. We found that the finite-time dynamics and thermodynamics of the cycle depend non-trivially on the different time scales at play. In particular, driving the WS at a time scale comparable to the resonance time of the bath enhances the performance of the cycle and allows for an efficiency higher than the efficiency of the quasistatic cycle, but still below the Carnot bound. However, by adding thermalization of the WS with the baths at the end of compression/expansion processes one recovers the conventional scenario in which efficiency decreases by speeding up the processes. In addition, the performance of the cycle is dependent on the compression/expansion speeds asymmetrically, which suggests new freedom in optimizing quantum heat engines. The maximum output power and the maximum efficiency are obtained almost simultaneously when the real-time endpoints of the compression/expansion processes are considered instead of the equilibrium thermal endpoint states. However, the net extractable work always declines by speeding up the drive.

1. Introduction

A flourishing research activity has developed recently around the understanding of the thermodynamic properties of quantum systems [1–4]. Special attention has been devoted to quantum heat engines and refrigerators triggered by both new theoretical questions and technological advancements in dynamical control of microscopic systems [5–16]. From the theoretical point of view a natural question is whether the quantumness of the working substance (WS) can be exploited to achieve better performances over the classical systems. The role of quantum effects has been investigated for example in [17–23]. It has been also ascertained that the creation of coherence between energy levels leads to inner friction and reduction of the extractable work [24–30]. Thus, the sole use of a quantum WS does not in general guarantee superiority over the classical counterparts [31]. The study of quantum thermal machines has relied mostly on the Markovian (Lindblad) description of open system dynamics, which guarantees non-negative entropy production rate and consistency with the second law of thermodynamics [5]. It has been shown that non-Markovian dynamics could lead to negative entropy production for the open system reduced state, however, the sum of the entropy change of the bath and the open system together is positive [32]. Besides

these studies, non-Markovianity has been found to influence the performance of the quantum heat engines [33], and, importantly, may also enhance the output power [34].

The usual four-stroke thermodynamic cycles between two thermal baths at temperatures T_h and T_c are composed of four strokes that connect the four fixed endpoints of the cycle. Depending on the physical settings, a cycle may work either as a heat to work transformer (engine) or a refrigerator. Considering a heat engine, it is well-known that the maximum efficiency for heat to work transformation is obtained when the cycle is quasistatic and the processes are reversible. The Carnot efficiency $\eta_C = 1 - T_c/T_h$ sets an upper bound on the achievable efficiency of an engine working between two thermal baths at the corresponding temperatures. Achieving the maximum efficiency with a quasistatic cycle carries the cost of losing the output power. Therefore, a trade-off between the power and the efficiency is usually found for a cycle running at finite times. Curzon and Ahlborn [35] reported that the efficiency at maximum power for a Carnot cycle is given by the simple expression $\eta_{CA} = 1 - \sqrt{T_c/T_h}$. The authors in reference [36] have derived an upper bound and a lower bound for the efficiency at maximum power of low-dissipation Carnot heat engines and showed that one recovers the Curzon–Ahlborn efficiency when the cycle includes symmetric dissipations during the two isotherms. A universal constraint for the power and efficiency of the low-dissipation Carnot heat engines is derived in reference [37] and the optimal cycle is introduced in [38]. In addition, geometric approaches to the trade-off between power and efficiency and optimization of the cycles is considered, e.g. in references [39, 40]. The engineering of finite-time processes have been also studied. For the finite-time coherent driving of the isolated WS the shortcut-to-adiabaticity approach provides a way to mimic the adiabatic process [41, 42]. This technique has been recently demonstrated experimentally with superconducting circuits [43, 44] and it was generalized to the case of driven open quantum systems [45]. The shortcut-to-adiabaticity has been employed, for example, to boost the performance of an Otto refrigerator [46] and an Otto heat engine [47]. The Otto cycle with a quantum WS has been extensively studied in the adiabatic as well as in the non-adiabatic case [12, 13, 16, 19, 21, 28, 34, 47].

Dealing with finite-time isothermal processes is more complicated, in comparison with finite-time adiabatic processes, due to the simultaneous driving of the WS and its coupling to the heat bath. Usually, to obtain the real-time dynamics of the WS during a finite-time isotherm a slow drive whose effect falls within the validity of the adiabatic limit is assumed, allowing one to ignore the non-adiabatic effects [48–50]. This assumption is relaxed in the derivation of a time-dependent Markovian master equation to capture non-adiabatic effects but retaining the assumption that the time scales of the external drive and the ones of the coupling to the bath are still well-separated [51]. Using this master equation, it has been proposed to reverse-engineer the thermalization to find a corresponding driving protocol which provides a shortcut to equilibration [52]. Alternatively, manipulating the coupling between the WS and the bath is also shown to speed-up isothermal strokes [53].

Carnot and Stirling cycles both include isothermal processes. Although finite-time Carnot cycle has been studied extensively to address the trade-off between power and efficiency, Stirling cycle has received much less attention. Stirling cycle has been studied in the ideal adiabatic regime [54, 55] and only very recently a finite-time scenario in an optomechanical implementation has been studied [56]. In particular, most of the previous studies dealing with both Carnot and Stirling cycles running in finite times are limited to phenomenological approaches and when the real-time dynamics of the WS is considered, they have been usually limited to the slow-driving or low-dissipation regime. In addition, it is assumed that all the four endpoints of the cycles are fixed, e.g. during an isotherm the WS can be driven out of the equilibrium but at the end of the process it will be eventually brought back to the fixed endpoint corresponding to the equilibrium state at the end of the protocol. But what should we except if we follow the real-time dynamics of the WS even at the end of the protocol, i.e. the endpoint of the isotherm be dependent on the real-time dynamics of the WS? In this case, the term 'isothermal' does not mean anymore that the WS has the same temperature at the beginning and at the end of the process. It would rather refer to the driving of the WS while it is connected to a thermal bath at a fixed temperature. In this work, we address the role of this deviation from the conventional endpoints of the isotherms in the performance of a finite-time Stirling cycle working as a heat engine with a qubit as the WS. Unlike the previous studies, here we consider the real-time dynamics of the WS beyond the slow-driving approximation using a non-Markovian master equation that allows for arbitrary fast driving.

We observe that the efficiency of the cycle depends on the interplay between the driving time, the correlation times of the baths and the resonance times of the baths. Interestingly, the efficiency exceeds that of a quasistatic cycle if we drive the WS at a time scale comparable to the resonance time of the baths. However, by forcing the WS to reach the thermal equilibrium at the end of the isotherms (having a conventional Stirling cycle with all four endpoints fixed), we recover the well-known behavior in which the efficiency always decreases by speeding up the processes. Interestingly, the average output power gets its

maximum almost at the same time scale of the driving at which the efficiency is maximum. This is however not true for the extractable work, which decreases as we speed up the drive. Our results also show that the performance of the cycle is non-trivially dependent on the durations of the compression and expansion strokes in an asymmetric way.

The paper is organized as follows: in section 2 we introduce the master equation, followed by the presentation of the Stirling engine in section 3. The calculation of work and heat for the Stirling engine is done in section 3. Section 4 deals with the evaluation of the thermodynamic performance of the engine. Finally, section 6 is devoted to concluding remarks.

2. The master equation

To study the dynamics of a driven WS in contact with a thermal bath we employ a non-Markovian master equation obtained by applying the approach developed in references [57, 58]. Assuming weak coupling to the baths and the Born approximation, a general time-convolutionless non-Markovian master equation is derived using the Nakajima–Zwanzig method. Such a master equation is valid for any characteristic time scale of the drive, e.g. the period in a periodic drive or the ramping time in the case of a switching. The master equation retains both rotating and counter-rotating contributions, where the latter is especially non-negligible at fast driving speeds. Here we introduce the operatorial form of the master equation and discuss its main features, leaving more details on the numerical implementation and how to recast the master equation in the adiabatic basis in appendix A.

Let us consider a quantum system subject to an external coherent driving field and weakly coupled to a thermal bath at an inverse temperature β. The total Hamiltonian reads ($\hbar = 1$)

$$\hat{H}(t) = \hat{H}_S(t) + \hat{H}_I(t) + \hat{H}_B, \tag{1}$$

where $\hat{H}_S(t)$ and $\hat{H}_B(t)$ are the bare Hamiltonian of the open system and the bath respectively. We write the interacting Hamiltonian in the form

$$\hat{H}_I(t) = \hat{S}(t) \otimes \hat{B}, \tag{2}$$

with $\hat{S}(t)$ being a time-dependent operator acting on the open system, and $\hat{B}$ an operator acting on the bath. The non-Markovian master equation reads [57]

$$\mathcal{L}_t[\hat{\rho}(t)] = -i[\hat{H}_S(t), \hat{\rho}(t)] + \int_0^t d\tau \left[\Phi(t - \tau)[\hat{\bar{S}}(t, \tau)\hat{\rho}(t), \hat{S}(t)] + \text{h.c} \right], \tag{3}$$

where

$$\hat{\bar{S}}(t, \tau) = \hat{U}(t, \tau)\hat{S}(\tau)\hat{U}(t, \tau)^\dagger, \tag{4}$$

$$\hat{U}(t, \tau) = \text{T} \, e^{-i \int_\tau^t ds \hat{H}_S(s)}, \tag{5}$$

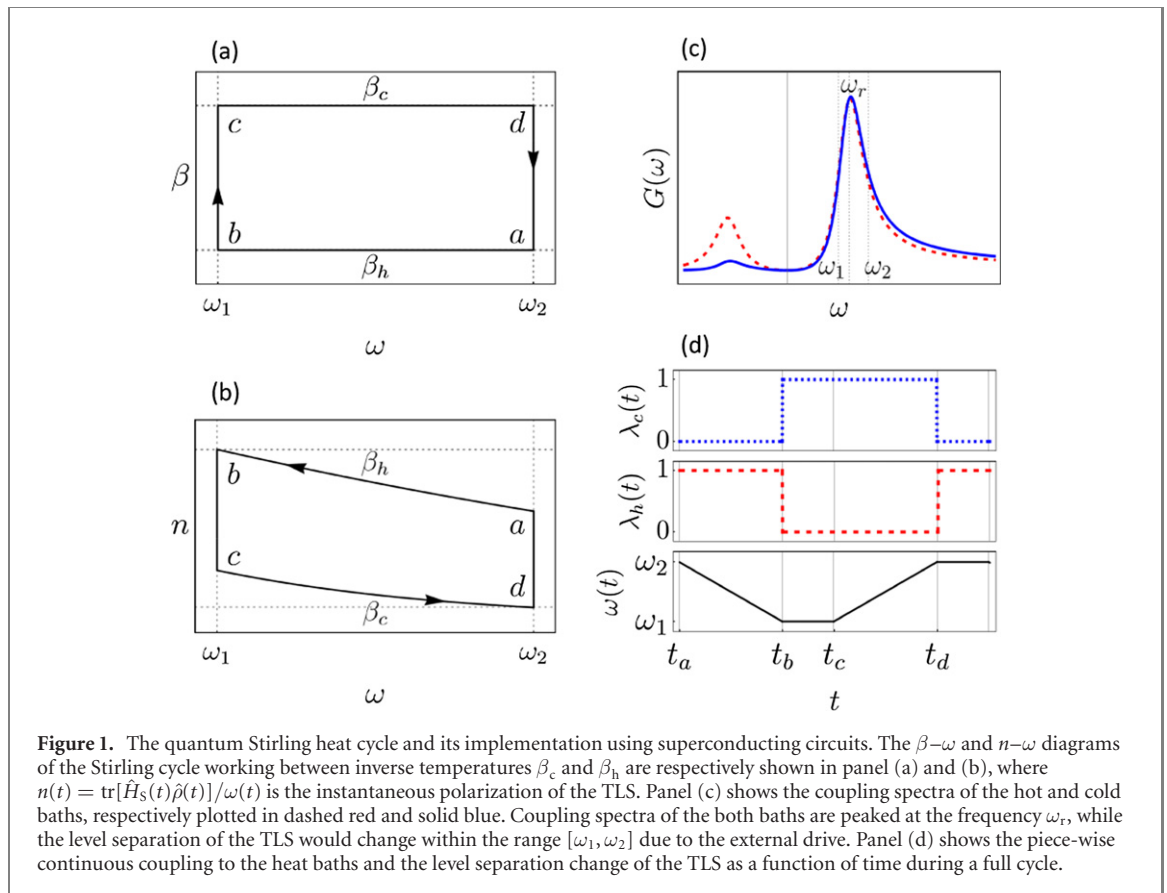$$\Phi(t) = \langle e^{i\hat{H}_B t} \hat{B} \, e^{-i\hat{H}_B t} \hat{B} \rangle_{\rho_B}. \tag{6}$$

Here $\Phi(t)$ is the correlation function of the bath and ρ_B denotes the equilibrium state of the bath at an inverse temperature β. The correlation function is related to the bath's coupling spectrum $G_\beta(\omega)$ via the Fourier transform $G_\beta(\omega) = \int_{-\infty}^{+\infty} ds \, \Phi(s) e^{i\omega s}$.

By decomposing the operators in the master equation w.r.t. the instantaneous eigenvectors of $\hat{H}_S(t)$, denoted by $\{|\epsilon_i(t)\rangle\}$, we get (see appendix A for more details)

$$\mathcal{L}_t[\hat{\rho}(t)] = -i \left[\hat{H}_{\text{eff}}(t), \hat{\rho}(t) \right] + \mathcal{D}_t^{(R)}[\hat{\rho}(t)] + \mathcal{D}_t^{(CR)}[\hat{\rho}(t)]. \tag{7}$$

where $\hat{H}_{\text{eff}}(t) = \hat{H}_S(t) + \hat{H}_L^{(R)}(t) + \hat{H}_L^{(CR)}(t)$ with $\hat{H}_L^{(\alpha)}(t)$ with $\alpha = \text{R, CR}$ is the rotating/counter-rotating Lamb shift in the energy levels of the system generated by the coupling to the bath. Also the non-unitary dissipators $\mathcal{D}_t^{(R)}[\cdot]$ and $\mathcal{D}_t^{(CR)}[\cdot]$ account for the exchange of energy with the bath and/or decoherence.

Note that the dissipators accounting for two different baths are additive by construction if one assumes that the baths are initially uncorrelated. Naturally, the specific expressions of the different terms appearing on the rhs of equation (7) depend on the choice of the free Hamiltonian of the system and more importantly on the coupling Hamiltonian $\hat{H}_I(t)$.

Figure 1. The quantum Stirling heat cycle and its implementation using superconducting circuits. The $\beta-\omega$ and $n-\omega$ diagrams of the Stirling cycle working between inverse temperatures β_c and β_h are respectively shown in panel (a) and (b), where $n(t) = \mathrm{tr}[\hat{H}_S(t)\hat{\rho}(t)]/\omega(t)$ is the instantaneous polarization of the TLS. Panel (c) shows the coupling spectra of the hot and cold baths, respectively plotted in dashed red and solid blue. Coupling spectra of the both baths are peaked at the frequency ω_r, while the level separation of the TLS would change within the range $[\omega_1, \omega_2]$ due to the external drive. Panel (d) shows the piece-wise continuous coupling to the heat baths and the level separation change of the TLS as a function of time during a full cycle.

3. Quantum Stirling heat engine

The Stirling cycle is composed of two isothermal strokes and two isochoric thermalizations. Classically it is common to supplement the cycle with two extra steps which involve the interaction of WS with the so-called regenerator. The latter is typically some substance with a very high heat capacity whose task is to absorb heat from the WS during the cooling isochoric stroke and transfer this heat back to the WS during the heating isochor to improve the overall efficiency and minimize the waste heat. In this work we do not consider a regenerative setup, i.e. the WS interacts directly with the heat baths instead of the regenerator. Considering a quasistatic Stirling cycle working as a heat engine that has four fixed endpoints *a*, *b*, *c*, and *d*, the diagrams for temperature and polarization versus level separation are depicted respectively in the panels (a) and (b) in figure 1, where the polarization is given by $n(t) = \mathrm{tr}[\hat{H}_S(t)\hat{\rho}(t)]/\omega(t)$. Assuming a two-level system (TLS) as the WS, the cycle is composed of four strokes:

(a) Isothermal compression, process $a \to b$, with duration τ_{ab}: the level separation of the TLS reduces from ω_2 to ω_1 while it is coupled to the hot bath at an inverse temperature β_h.

(b) Isochoric thermalization, process $b \to c$, with duration τ_{bc}: the TLS is disconnected from the hot bath and is brought to contact with the cold bath at an inverse temperature β_c, with which it thermalizes while the external drive is off.

(c) Isothermal expansion, process $c \to d$, with duration τ_{cd}: the level separation of the TLS increases from ω_1 back to ω_2 while it is still coupled to the cold bath.

(d) Isochoric thermalization, process $d \to a$, with duration τ_{da}: the TLS is disconnected from the cold bath and is brought back to contact with the hot bath. The TLS thermalizes while driving is off.

Note that the durations of isothermal processes 1 and 3, denoted respectively by τ_{ab} and τ_{cd}, are very large when the cycle is quasistatic. Slow processes allow the WS to maintain the isothermal trajectories depicted in the panels (a) and (b) in figure 1. However, in a finite-time cycle the processes have finite nonzero speeds and the total duration of a full cycle is then $T = \tau_{ab} + \tau_{bc} + \tau_{cd} + \tau_{da}$. Depending on the speed of processes 1 and 3, the trajectory of the WS may deviate from the isothermal ones. In particular, this deviation leads the WS to end up at different endpoints rather than the equilibrium points *b* and *d* depicted in the panels (a) and (b) of figure 1. Usually, it is assumed that at the end of isotherms the WS is eventually brought back to the equilibrium states (points *b* and *d*) to fulfill the isothermal constraint that

Table 1. Definitions and values of the relevant physical parameters used in this work. Note that ω_0 is the reference energy scale of the TLS, with respect to which we normalize all other frequencies and time scales. ($\hbar = 1$, $k_B = 1$).

Parameter	Definition	Value
τ_R	Relaxation time of the TLS	$1/G_{\beta_i g_i}(\omega_r)$
τ_B	Resonance time of the bath	$2\pi/\omega_r$
τ_C	Correlation time of the bath	Controlled by f
β_h	Inverse temperature of the hot bath	$2/\omega_0$
β_c	Inverse temperature of the cold bath	$5/\omega_0$
(g_c, g_h)	Set of TLS-bath coupling amplitudes	$g_1 = (0.2, 0.17)$ or $g_2 = \sqrt{2} \times g_1$
ω_r	Resonance frequency of the baths	$0.6 \times \omega_0$
ω_1	Minimum frequency of the TLS	$0.49 \times \omega_0$
ω_2	Maximum frequency of the TLS	$0.78 \times \omega_0$
f	Quality factor of the bath's resonators	2 or 3
τ_D	Unit of driving duration	$\tau_R(g_1)$
τ_{th}	Duration of the isochoric strokes	$6 \times \tau_R(g_1)$
Δ	Static part of the TLS Hamiltonian	0.12

the WS has at least the same temperatures at the beginning and at the end of the process. Here, we let the WS keep its real-time endpoint at the end of the isotherms, so we skip the conventional isothermal constraint. In what follows we present a Hamiltonian model to implement the aforementioned cycle. Using the derived master equation we obtain the real-time dynamics of the WS and investigate the role of the deviation from the equilibrium endpoints in the performance of the Stirling cycle.

3.1. The model

We present here the Hamiltonian model used in this work and give more details about a possible implementation of this model using superconducting circuits in appendix B. The free Hamiltonian of the TLS and the TLS-bath coupling Hamiltonian are respectively denoted by $\hat{H}_S(t)$ and $\hat{H}_{I,\alpha}(t)$, given by

$$\hat{H}_S(t) = \omega_0[q(t)\hat{\sigma}_z + \Delta\hat{\sigma}_x], \qquad \hat{H}_{I,\alpha}(t) = \lambda_\alpha(t)\hat{\sigma}_y \otimes \hat{B}_\alpha. \tag{8}$$

Here ω_0 denotes a reference energy scale for the non-driven qubit. The operator $\hat{B}_\alpha$ acts on the cold/hot bath, with $\alpha = c, h$, and incorporates the coupling amplitudes between the WS and the corresponding bath. It is worth mentioning that without loss of generality of the results, one can also consider the coupling to the baths along $\hat{\sigma}_x$.

As depicted in the panel (d) of figure 1, we choose the driving protocol $q(t)$ such that the instantaneous level separation $\omega(t) = 2\omega_0\sqrt{q(t)^2 + \Delta^2}$ of the TLS changes linearly with time within the interval $[\omega_1, \omega_2]$ with a given constant speed. This requirement fixes unambiguously $q(t) = \sqrt{\omega(t)^2/4 - \Delta^2}$. A relevant coupling spectrum for the baths regarding the setup considered in this work is shown in the panel (c) of figure 1 and takes a specific expression given by [46]

$$G_{\beta_i g_i}(\omega \geqslant 0) = \frac{g_i^2}{1 + f_i^2\left(\frac{\omega}{\omega_i} - \frac{\omega_i}{\omega}\right)^2} \times \frac{\omega}{1 - e^{-\beta_i\omega}}. \tag{9}$$

With $i = c, h$ denoting again the cold and hot baths, the coupling strengths to the baths are described by g_i, the resonance frequencies of the baths are denoted by ω_i, and f_i are the quality factors of the baths resonators which, determine the width of the spectra of the baths. We assume identical resonance frequency for the two baths denoted by ω_r and set the values of coupling strengths g_c and g_h such that the corresponding spectra have the same amplitudes at ω_r (see panel (c) of figure 1). All the relevant physical parameters and their values used in this work are reported in table 1.
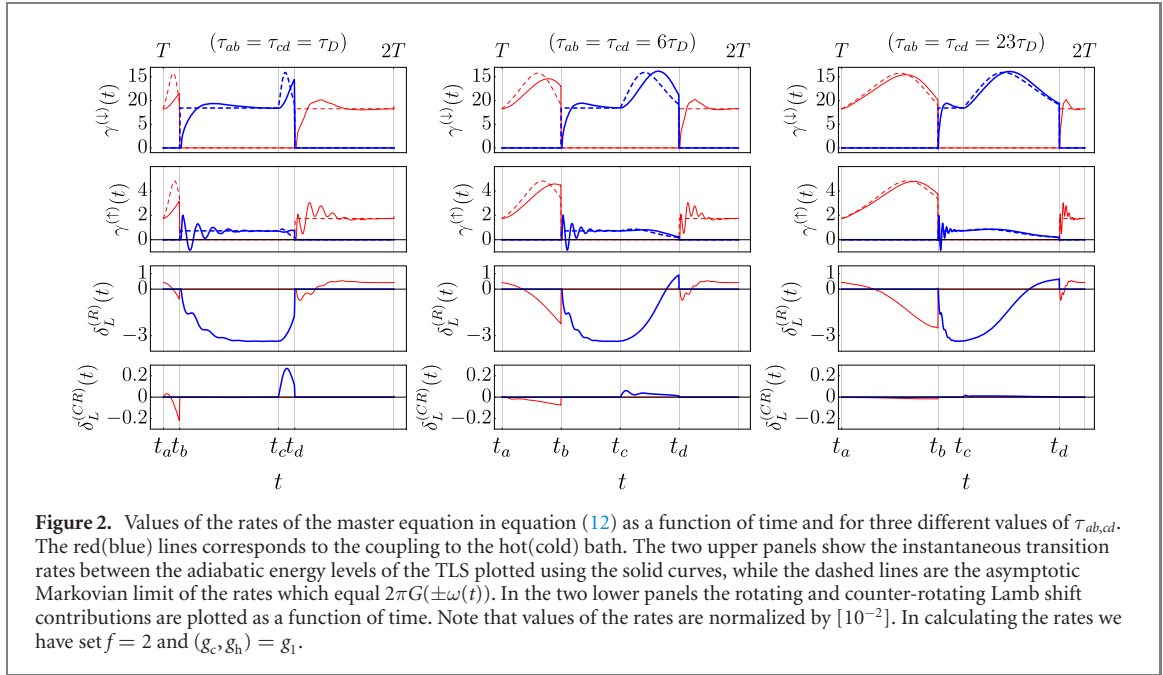
3.2. Real-time dynamics

With the specific Hamiltonian given in equation (8), the instantaneous energy basis of the TLS reads

$$|\epsilon_e(t)\rangle = \cos\theta_t |e\rangle + \sin\theta_t |g\rangle, \tag{10}$$

$$|\epsilon_g(t)\rangle = \sin\theta_t |e\rangle - \cos\theta_t |g\rangle, \tag{11}$$

with $\theta_t = (1/2)\cot^{-1}(q(t)/\Delta)$ and $|e(g)\rangle$ as the eigenbasis of $\hat{\sigma}_z$ Pauli operator. By defining the transition operator $\hat{L}(t) = |\epsilon_g(t)\rangle \langle\epsilon_e(t)|$ between the instantaneous energy basis of the TLS, the master equation in

Figure 2. Values of the rates of the master equation in equation (12) as a function of time and for three different values of $\tau_{ab,cd}$. The red(blue) lines corresponds to the coupling to the hot(cold) bath. The two upper panels show the instantaneous transition rates between the adiabatic energy levels of the TLS plotted using the solid curves, while the dashed lines are the asymptotic Markovian limit of the rates which equal $2\pi G(\pm\omega(t))$. In the two lower panels the rotating and counter-rotating Lamb shift contributions are plotted as a function of time. Note that values of the rates are normalized by $[10^{-2}]$. In calculating the rates we have set $f = 2$ and $(g_c, g_h) = g_1$.

equation (7) takes the form

$$
\mathcal{L}_t[\hat{\rho}(t)] = -i\left[\left(1 + \delta_L^{(R)}(t)\right)\hat{H}_S(t) + \delta_L^{(CR)}(t)\left(\Delta\hat{\sigma}_z - q(t)\hat{\sigma}_x\right), \hat{\rho}(t)\right]
$$

$$
+ \gamma^{(\downarrow)}(t)\left[\hat{L}(t)\hat{\rho}(t)\hat{L}^\dagger(t) - \frac{1}{2}\{\hat{L}^\dagger(t)\hat{L}(t), \hat{\rho}(t)\}\right]
$$

$$
+ \gamma^{(\uparrow)}(t)\left[\hat{L}^\dagger(t)\hat{\rho}(t)\hat{L}(t) - \frac{1}{2}\{\hat{L}(t)\hat{L}^\dagger(t), \hat{\rho}(t)\}\right] + \mathcal{D}_t^{(CR)}[\hat{\rho}(t)]. \tag{12}
$$

Here the Lamb shift contributions in the unitary part of the evolution are given by

$$
\hat{H}_L^{(R)}(t) = \delta_L^{(R)}(t)\hat{H}_S(t), \qquad \hat{H}_L^{(CR)}(t) = \delta_L^{(CR)}(t)\left(\Delta\hat{\sigma}_z - q(t)\hat{\sigma}_x\right), \tag{13}
$$

and the rotating part of the dissipator ($\mathcal{D}_t^{(R)}$) is in the Lindblad form, with the time-dependent transition rates $\gamma^\uparrow(t), \gamma^\downarrow(t)$ and the operator $L(t)$. Derivation of the energy shifts $\delta_L^{(i)}(t)$ and also the transition rates $\gamma^\uparrow(t), \gamma^\downarrow(t)$ are given in appendix A.2. An analytic expression for the counter-rotating dissipator $\mathcal{D}_t^{(CR)}[\cdot]$ is, however, too cumbersome to be included. According to expressions in equation (13), the rotating Lamb shift contribution is proportional to $\hat{H}_S(t)$, whereas, the counter-rotating one does not commute with $\hat{H}_S(t)$. Temporal behavior of the transition rates $\gamma^\uparrow(t), \gamma^\downarrow(t)$ and also the Lamb shifts are shown in figure 2 for different compression and expansion speeds during the isothermal branches. Note that in this figure, and also the rest of the paper, we consider a scale for the driving duration denoted by τ_D. Recalling that the amplitude of the spectra of the cold and hot baths are set to be identical at the resonance frequency ω_r, the value of τ_D is fixed to the relaxation time of the TLS when the coupling amplitudes are $(g_c = 0.2, g_h = 0.17)$, thus $\tau_D := \tau_R(g_1)$. In addition, the durations of the isochoric branches are always fixed at $\tau_{th} = 6 \times \tau_R(g_1)$. The temporal behavior of counter-rotating Lamb shift is presented in the lower panel of figure 2. We observe that the amplitude of the counter-rotating shifts decrease by slowing down the processes. In the two upper panels of figure 2, we have plotted the amplitude of the transition rates $\gamma^\uparrow(t), \gamma^\downarrow(t)$ as a function of time and using solid lines. The dashed lines, represent the Markovian limit of the rates given by $2\pi G_\beta(\pm\omega(t))$ [58]. One sees that it is only for the asymptotic slow driving (adiabatic limit) that the rates $\gamma^{(\uparrow)}(t)$ and $\gamma^{(\downarrow)}(t)$ approach to their Markovian limits.

In this work, we include all the terms in equation (12) to calculate the evolution of the TLS. However, it is worth discussing how the evolution behaves if we only take the rotating terms into account (excluding $\mathcal{D}_t^{(CR)}$ and $\hat{H}_L^{(CR)}$ in equation (12)). In this case, we get a time-dependent master equation in the Linblad form, with respect to the operator $\hat{L}(t)$, which we denote by $\mathcal{L}_t^{(R)}[\hat{\rho}(t)]$. This master equation contains the non-adiabatic contributions (due to the memory kernel) and allows one to realize what is missed by assuming an adiabatic Markovian master equation. Consider $\mathcal{L}_t^{(R)}$ at a given fixed time $t = \tau$ denoted by $\mathcal{L}_\tau^{(R)}$, which means all the rates, Hamiltonian, and jump operators are set to their configuration at $t = \tau$ and

remain unchanged for $t > \tau$. We define the invariant state of this generator by $\hat{\rho}_{\text{eq}}^{(R)}(\tau)$, such that $\mathcal{L}_{\tau}^{(R)}[\hat{\rho}_{\text{eq}}^{(R)}(\tau)] = 0$. It is straightforward to check that the invariant state is given by

$$\hat{\rho}_{\text{eq}}^{(R)}(\tau) = \Gamma(\tau)^{-1} \left[\gamma^{(\uparrow)}(\tau) \left| \epsilon_e(\tau) \right\rangle \left\langle \epsilon_e(\tau) \right| + \gamma^{(\downarrow)}(\tau) \left| \epsilon_g(\tau) \right\rangle \left\langle \epsilon_g(\tau) \right| \right], \tag{14}$$

with $\Gamma(\tau) = \gamma^{(\uparrow)}(\tau) + \gamma^{(\downarrow)}(\tau)$. We stress that due to the explicit time dependency of the decay rates, $\hat{\rho}_{\text{eq}}^{(R)}(\tau)$ is not necessarily identical to a Gibbs state at the same temperature of the heat bath. Only for the asymptotic slow driving (adiabatic limit) the decay rates $\gamma^{(\uparrow)}(\tau)$ and $\gamma^{(\downarrow)}(\tau)$ approach to their Markovian limits $2\pi G_{\beta}(\pm\omega(\tau))$ and one consequently gets the equilibrium state $\rho_{\text{eq}}(\beta,\tau) = \exp(-\hat{H}_S(\tau)\beta)/\text{tr}[\exp(-\hat{H}_S(\tau)\beta)]$, where β is the inverse temperature of the bath with whom the TLS interacts. The asymptotic state of the evolution due to the full generator $\mathcal{L}_t$—which includes the counter-rotating terms—is, however, more complicated and does not depend solely on the rates $\gamma^{(\uparrow/\downarrow)}(t)$. Consider the full generator at a given fixed time $t = \tau$ denoted by $\mathcal{L}_{\tau}$. We define its asymptotic state formally by $\hat{\rho}_{\tau}^* = \lim_{t\to\infty} \left[\exp(t\mathcal{L}_{\tau})\hat{\rho}_i \right]$, where $\hat{\rho}_i$ is some initial input state. We now proceed to utilize these tools to characterize the Stirling cycle used as a heat engine.

The periodicity of the cycle requires that both the state of the WS and the generator of the open dynamics at the end of a period reset to their initial configurations, i.e. $\hat{\rho}(t + nT) = \hat{\rho}(t)$ and $\mathcal{L}_{t+nT} = \mathcal{L}_t$. According to the numerical results in this work, by excluding the first cycle with $0 \leqslant t < T$ we meet this constraint. Moreover, the duration of isochoric strokes are set sufficiently large ($\tau_{bc} = \tau_{da} = 6 \times \tau_{\text{R}}(g_1)$) such that the TLS can reach its asymptotic equilibrium states at the end of $b \to c$ and $d \to a$ branches. Accordingly, the two points a and c are always fixed in our analysis, as shown in the panel (a) of figure 3. Nonetheless, we consider arbitrary duration for the isothermal strokes. If the driving is sufficiently slow, the WS remains in an instantaneous equilibrium state with the bath during the whole process. This ideal case corresponds to the ab and cd trajectories in the panel (a) of figure 3. However, a faster drive kicks the WS out of the manifold of equilibrium states and, consequently, its trajectory deviates from the ideal isothermal (quasistatic) ones. The opposite regime is when the drive is so fast that the dynamics of the WS is essentially diabatic and its state remains unchanged during the process. Therefore, at the end of the diabatic process we end up at the point $\bar{b}(\bar{d})$, instead of equilibrium endpoints $b(d)$. Let us now define the real-time target points of the WS at the end of the compression and expansion processes with some arbitrary speeds, respectively by b' and d'. The corresponding points of the asymptotic (equilibrium) states $\hat{\rho}_{t_b}^*$ and $\hat{\rho}_{t_d}^*$ of the WS at the end of the processes are also denoted by b^* and d^*. Therefore, as it is shown in the panels (b)–(d) of figure 3, by increasing the speed of driving one changes the trajectory of the WS within the two areas $a\bar{b}b$ and $c\bar{d}d$, moving from the isothermal trajectories towards the diabatic ones. Within this general picture, we now study in detail how different speeds affect the thermodynamic performance of the Stirling heat engine.

4. Thermodynamic performance

Studying the performance of the heat engine requires to calculate the work done as well as the energy exchanged with the baths during each stroke of a full cycle. To do so, we have two options here: using the bare Hamiltonian $H_S(t)$ in equation (8) or the effective Hamiltonian given by

$$\hat{H}_{\text{eff}}(t) = \hat{H}_S(t) + \sum_{\alpha=c,h} \left[\delta_{\text{L}}^{(R,\alpha)}(t)\hat{H}_S(t) + \delta_{\text{L}}^{(CR,\alpha)}(t) \left(\Delta\hat{\sigma}_z - q(t)\hat{\sigma}_x \right) \right], \tag{15}$$

where the summation is over the terms corresponding to the hot and the cold baths. On the one hand, using the effective Hamiltonian allows for making a full separation between the energies that are locally accessible to the WS and the baths [59] and, on the other hand, one may argue that since we only have control on the external field, so the energies should be calculated using the bare Hamiltonian. In what follows we present some of our results considering both of the two cases to show the possible contribution of the Lamb shifts. The full dissipator acting on the WS has two parts each corresponding to one of the baths:

$$\mathcal{D}_t[\cdot] = \mathcal{D}_t^{(c)}[\cdot] + \mathcal{D}_t^{(h)}[\cdot], \tag{16}$$

Let us for the sake of simplicity of the notations denote the Hamiltonian of the WS, whether the bare Hamiltonian or the effective one, by $H_S(t)$.

Having the Hamiltonian and the dissipator of the dynamics, we can calculate the average of work and heat transferred. For the average work done on the WS in the time interval $[t_1, t_2]$ one has (considering ω_0 for the unit of energy)

$$\langle W(t_1, t_2) \rangle = \int_{t_1}^{t_2} \text{d}s \, \text{tr} \left[\left(\frac{\text{d}}{\text{d}t} \hat{H}_S(t)|_{t=s} \right) \hat{\rho}(s) \right], \tag{17}$$

Figure 3. Polarization–frequency diagram of the Stirling cycle. In panel (a) an ideal slow cycle is plotted using the dashed grey lines which follows the isothermal trajectories *ab* and *cd*, whereas the fast diabatic trajectories are depicted by $a\bar{b}$ and $c\bar{d}$ in dashed red. In the rest of the panels ab' and cd' denote the real-time trajectories with finite time compression and expansion and considering three different duration. Also, ab^* and cd^* trajectories plotted in dashed orange denote the asymptotic steady state of the dynamics.

which relates to the average output power $P(t_1, t_2)$ during this time interval via

$$P(t_1, t_2) = (t_2 - t_1)^{-1} \langle W(t_1, t_2) \rangle. \tag{18}$$

We notice that using the effective Hamiltonian has non-trivial consequences. Specifically, if the Lamb shifts vary in time (which indeed happens here due to presence of a memory kernel in the master equation) it is possible to have non-zero work even when the external drive is off. Furthermore, the average heat transferred into the WS in the time interval $[t_1, t_2]$ is given by
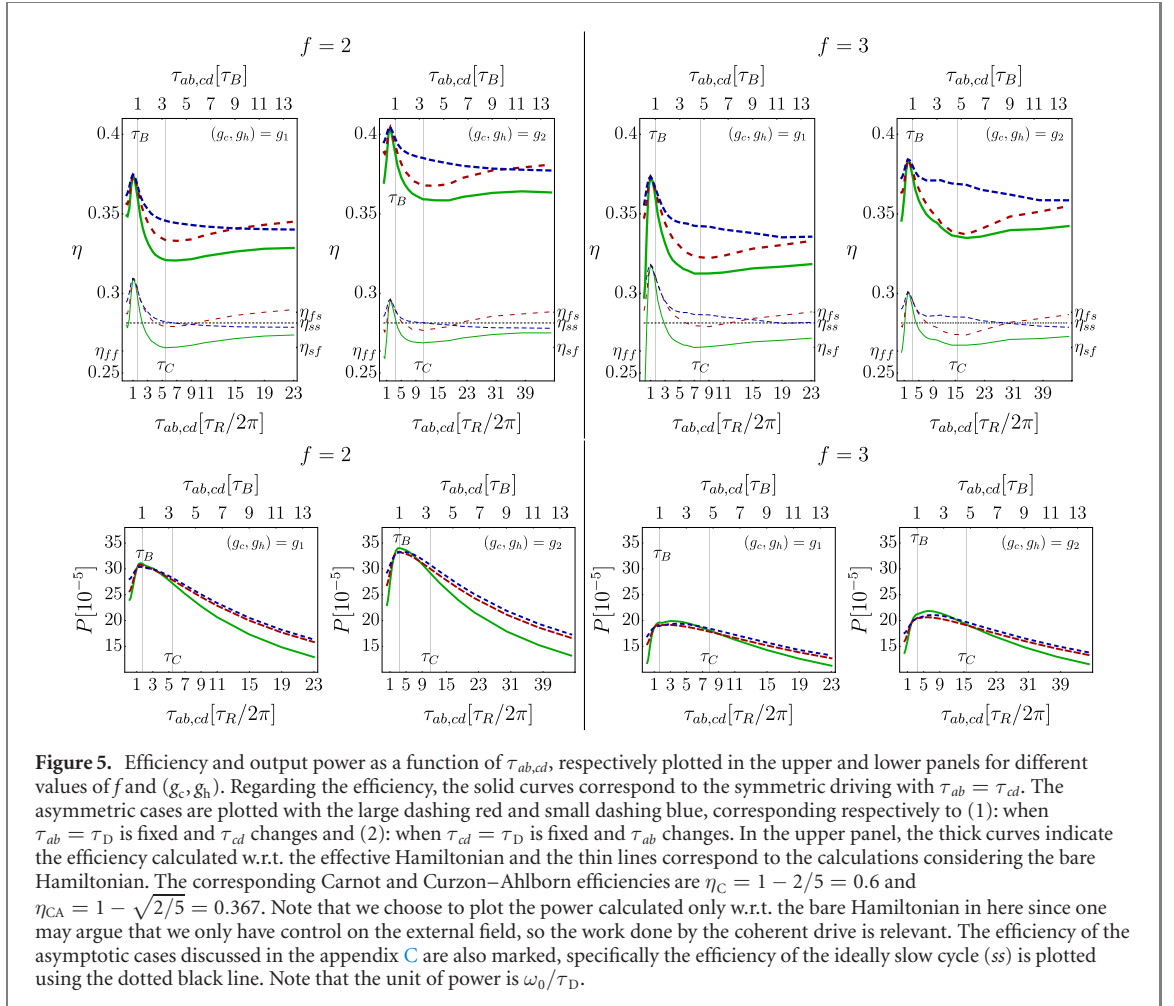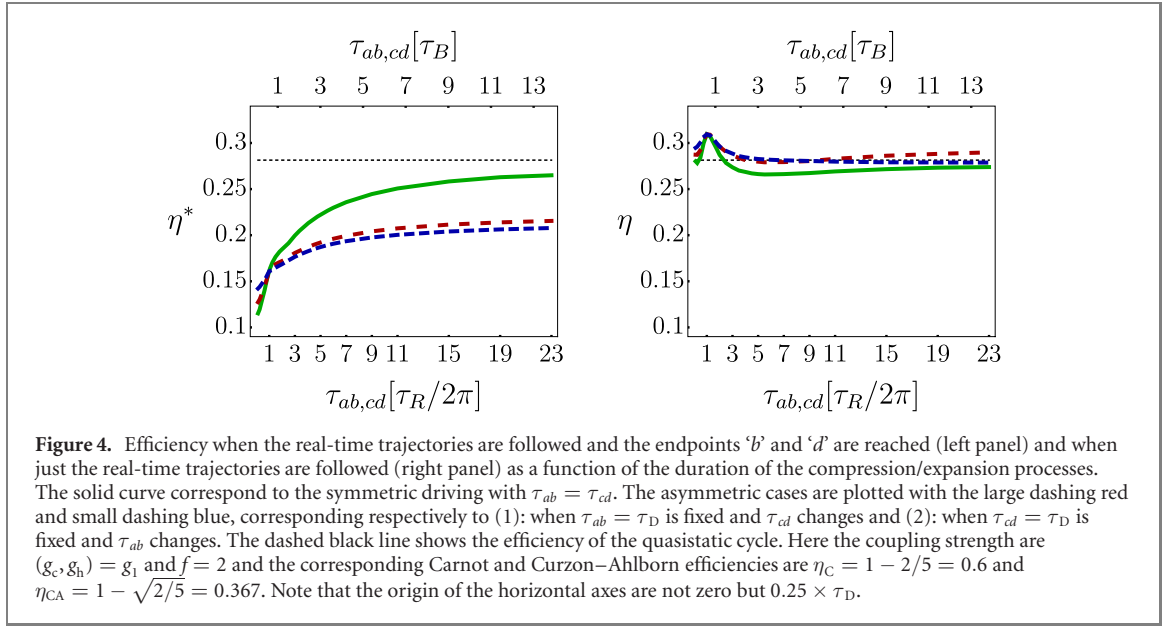
$$\langle Q(t_1, t_2) \rangle = \int_{t_1}^{t_2} \mathrm{d}s \ \mathrm{Tr} \left[\hat{H}_{\mathrm{S}}(s) \mathcal{D}_s[\hat{\rho}(s)] \right]. \tag{19}$$

By denoting $\langle W \rangle_{\mathrm{net}}$ as the average net extractable work during a full cycle, according to the first law of thermodynamics one has $\langle W \rangle_{\mathrm{net}} = -\langle Q \rangle_{\mathrm{net}}$, where $\langle Q \rangle_{\mathrm{net}}$ is the net average heat transferred. Consider the net positive heat transferred into the WS labeled by $\langle Q \rangle_{\mathrm{h}}$, then the efficiency of the cycle is determined by

$$\eta = \frac{\langle W \rangle_{\mathrm{net}}}{\langle Q \rangle_{\mathrm{h}}}. \tag{20}$$
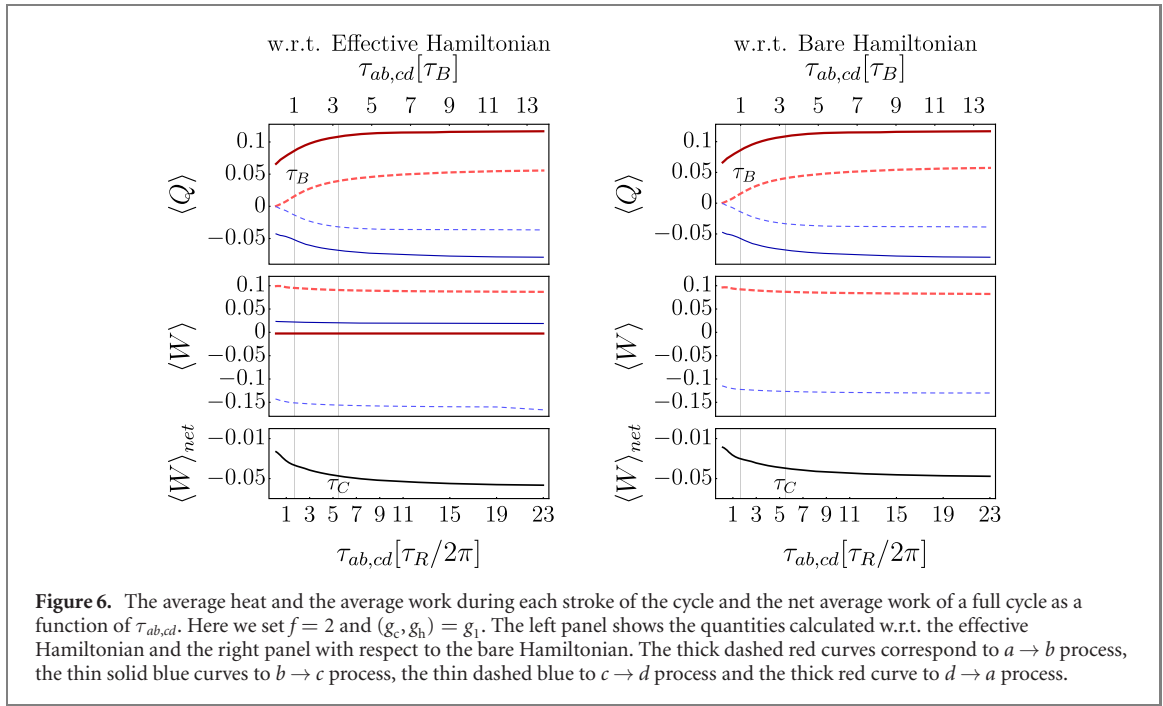
Remark 1: let us recall that in a regenerative Stirling heat engine the heat transferred during the isochoric branch $d \to a$ is not included in calculating the efficiency, since the regenerator is an internal component of the engine. However, here we let the WS interact directly with the hot bath during the stroke. Therefore, the net positive heat transferred into the WS has contributions both from the $a \to b$ and $d \to a$ branches.

Remark 2: before presenting our numerical results, we note that by considering the bare Hamiltonian $\hat{H}_{\mathrm{S}}(t)$ (excluding the Lamb shifts) one can provide analytic expressions of the efficiency regarding four limiting cases. As depicted in the panel (a) of figure 3, these case are: (*abcda*) trajectory corresponding to the ideal quasistatic processes—($a\bar{b}c\bar{d}a$) trajectory which follows the diabatic passage—($abc\bar{d}a$) trajectory corresponding to the quasistatic compression and diabatic expansion processes—and finally ($a\bar{b}cda$) trajectory which follows the diabatic compression and quasistatic expansion processes. We call these cases respectively (*ss*), (*ff*), (*sf*), (*fs*), with *s* and *f* denoting *slow* and *fast*, respectively. The analytic analysis of efficiency for these cases is presented in appendix B. Our aim is to examine the performance of the heat cycle for the situations between these four limiting cases and by considering the real-time evolution of the WS in finite times.

Figure 4. Efficiency when the real-time trajectories are followed and the endpoints 'b' and 'd' are reached (left panel) and when just the real-time trajectories are followed (right panel) as a function of the duration of the compression/expansion processes. The solid curve correspond to the symmetric driving with $\tau_{ab} = \tau_{cd}$. The asymmetric cases are plotted with the large dashing red and small dashing blue, corresponding respectively to (1): when $\tau_{ab} = \tau_D$ is fixed and τ_{cd} changes and (2): when $\tau_{cd} = \tau_D$ is fixed and τ_{ab} changes. The dashed black line shows the efficiency of the quasistatic cycle. Here the coupling strength are $(g_c, g_h) = g_1$ and $f = 2$ and the corresponding Carnot and Curzon–Ahlborn efficiencies are $\eta_C = 1 - 2/5 = 0.6$ and $\eta_{CA} = 1 - \sqrt{2/5} = 0.367$. Note that the origin of the horizontal axes are not zero but $0.25 \times \tau_D$.

Figure 5. Efficiency and output power as a function of $\tau_{ab,cd}$, respectively plotted in the upper and lower panels for different values of f and (g_c, g_h). Regarding the efficiency, the solid curves correspond to the symmetric driving with $\tau_{ab} = \tau_{cd}$. The asymmetric cases are plotted with the large dashing red and small dashing blue, corresponding respectively to (1): when $\tau_{ab} = \tau_D$ is fixed and τ_{cd} changes and (2): when $\tau_{cd} = \tau_D$ is fixed and τ_{ab} changes. In the upper panel, the thick curves indicate the efficiency calculated w.r.t. the effective Hamiltonian and the thin lines correspond to the calculations considering the bare Hamiltonian. The corresponding Carnot and Curzon–Ahlborn efficiencies are $\eta_C = 1 - 2/5 = 0.6$ and $\eta_{CA} = 1 - \sqrt{2/5} = 0.367$. Note that we choose to plot the power calculated only w.r.t. the bare Hamiltonian in here since one may argue that we only have control on the external field, so the work done by the coherent drive is relevant. The efficiency of the asymptotic cases discussed in the appendix C are also marked, specifically the efficiency of the ideally slow cycle (*ss*) is plotted using the dotted black line. Note that the unit of power is ω_0/τ_D.

4.1. Comparing two situations: (i) following the real-time trajectories plus enforcing the equilibrium endpoints 'b' and 'd', (ii) following real-time trajectories only

We first discuss the usual situation in which at the end of the isotherms the TLS is brought back to the equilibrium state with the baths (considering the bare Hamiltonian of the TLS). At the end of the $a \to b'$ process the TLS is at the state $\hat{\rho}_{b'} := \hat{\rho}(t_b)$, whereas the fixed endpoint b corresponds to the Gibbs state $\hat{\rho}_b := e^{-\beta_h \hat{H}(t_b)} / \mathrm{Tr}[e^{-\beta_h \hat{H}(t_b)}]$. Also, at the end of the $c \to d'$ process the TLS is at the state $\hat{\rho}_{d'} := \hat{\rho}(t_d)$,

Figure 6. The average heat and the average work during each stroke of the cycle and the net average work of a full cycle as a function of $\tau_{ab,cd}$. Here we set $f = 2$ and $(g_c, g_h) = g_1$. The left panel shows the quantities calculated w.r.t. the effective Hamiltonian and the right panel with respect to the bare Hamiltonian. The thick dashed red curves correspond to $a \to b$ process, the thin solid blue curves to $b \to c$ process, the thin dashed blue to $c \to d$ process and the thick red curve to $d \to a$ process.

whereas the fixed endpoint d corresponds to the Gibbs state $\hat{\rho}_d := e^{-\beta_c \hat{H}(t_d)} / \text{Tr}[e^{-\beta_c \hat{H}(t_d)}]$. Therefore, at the end of the compression process we need to apply the extra step $b' \to b$ to let the TLS thermalize with the hot bath. This means that the extra heat $Q_{b' \to b} = \text{Tr}[\hat{H}_S(t_b)(\hat{\rho}_b - \hat{\rho}_{b'})]$ has to be absorbed from the hot bath. On the other hand, since the TLS is now at the point b, when connected to the cold bath the same amount of heat has to be dissipated into the cold bath in order to go back to the point b'. The same situation also happens for the expansion process: the amount of heat $Q_{d' \to d} = \text{Tr}[\hat{H}_S(t_d)(\hat{\rho}_d - \hat{\rho}_{d'})]$ has to be dissipated into the cold bath to reach the fixed endpoint d and the same amount of heat has to be absorbed from the hot bath later to reach the point d' again. Considering this situation, the network and the heat absorbed from the hot bath during the cycle $a \to b' \to b \to c \to d' \to d \to a$ are given by

$$\langle W \rangle_{\text{net}}^* = -(Q_{a \to b'} + Q_{b' \to b} + Q_{b \to b'} + Q_{b' \to c} + Q_{c \to d'} + Q_{d' \to d} + Q_{d \to d'} + Q_{d' \to a}), \tag{21}$$

$$\langle Q \rangle_h^* = Q_{a \to b'} + Q_{b' \to b} + Q_{d' \to a} - Q_{d' \to d}. \tag{22}$$

However, without including the extra thermalization steps the work and the heat absorbed will be given by

$$\langle W \rangle_{\text{net}} = -(Q_{a \to b'} + Q_{b' \to c} + Q_{c \to d'} + Q_{d' \to a}), \tag{23}$$

$$\langle Q \rangle_h = Q_{a \to b'} + Q_{d' \to a}. \tag{24}$$
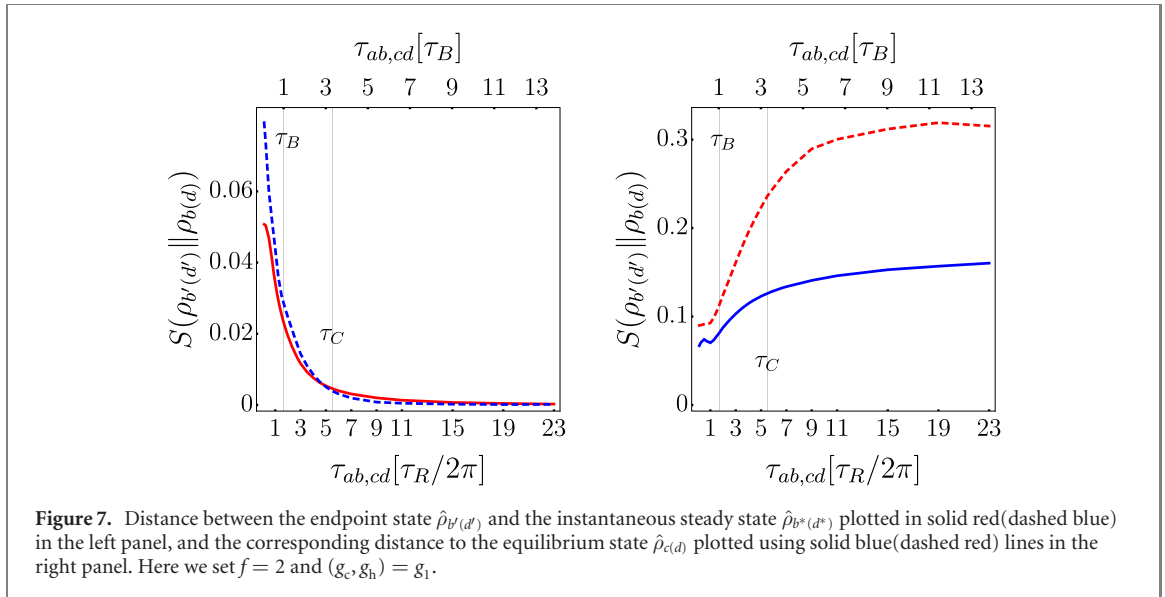
Since $Q_{b' \to b} = -Q_{b \to b'}$ and $Q_{d' \to d} = -Q_{d \to d'}$, one has $\langle W \rangle_{\text{net}}^* \equiv \langle W \rangle_{\text{net}}$. Therefore, enforcing thermal equilibrium at the end of the isotherms does not have an effect on the amount of extractable work. Nonetheless, the efficiency will be different. Considering the real-time dynamics of TLS, the efficiency reads

$$\eta = \frac{\langle W \rangle_{\text{net}}}{Q_{a \to b'} + Q_{d' \to a}}, \tag{25}$$

whereas, when we enforce thermalization at the end of isotherms the efficiency is

$$\eta^* = \frac{\langle W \rangle_{\text{net}}}{Q_{a \to b'} + Q_{b' \to b} + Q_{d' \to a} - Q_{d' \to d}}. \tag{26}$$

To compare η and η^* one should find the sign of the quantity $\Delta Q = Q_{b' \to b} - Q_{d' \to d}$. The two quantities η^* and η are plotted respectively in the left and right panels of figure 4 versus the duration of the processes and regarding both identical speeds of compression and expansion and the asymmetric cases with different speeds. The efficiency η^* shows a familiar behavior: it goes down by speeding up the processes, while it approaches the maximum value when the cycle is quasistatic. Interestingly, we see that the efficiency for the two asymmetric cases is not the same. It is worth mentioning that such an asymmetric behavior is also reported for the efficiency of the Carnot engine in the low-dissipation regime in reference [36]. On the other hand, the efficiency η corresponding to the real-time trajectories shows a very interesting
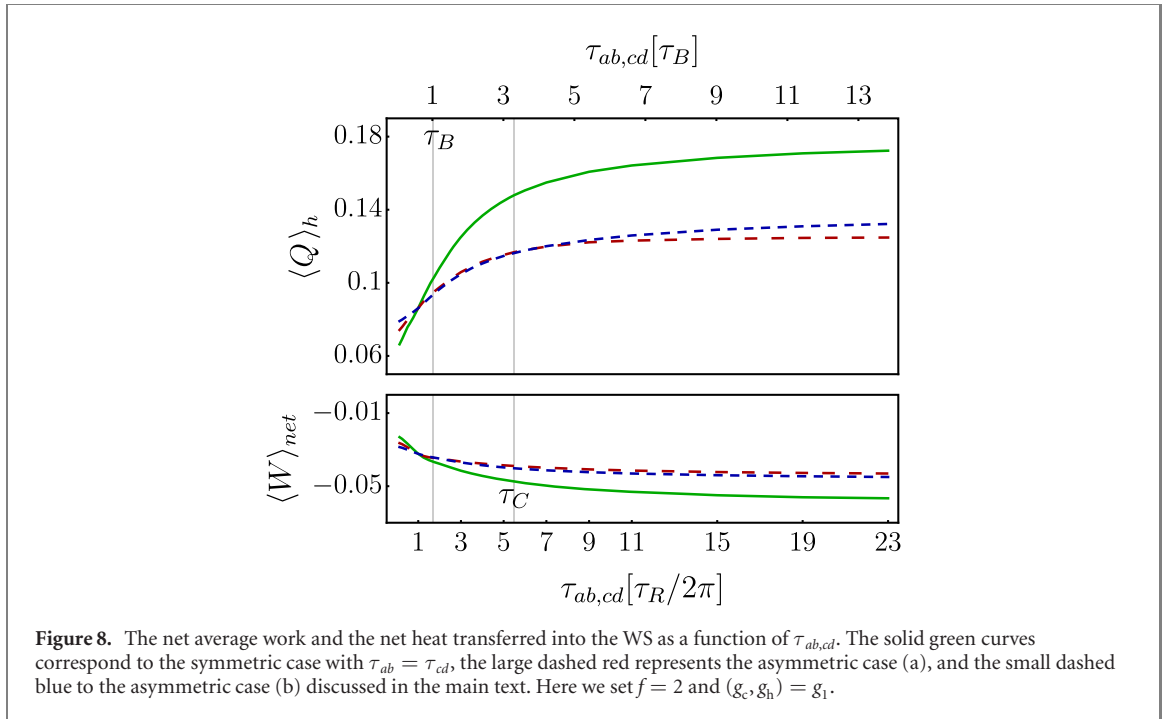
Figure 7. Distance between the endpoint state $\hat{\rho}_{b'(d')}$ and the instantaneous steady state $\hat{\rho}_{b^*(d^*)}$ plotted in solid red(dashed blue) in the left panel, and the corresponding distance to the equilibrium state $\hat{\rho}_{c(d)}$ plotted using solid blue(dashed red) lines in the right panel. Here we set $f = 2$ and $(g_c, g_h) = g_1$.

advantageous at faster driving speeds. We note that for quasistatic scenario the difference between η^* and η vanishes because the real-time endpoints b' and d' approaches to the equilibrium endpoints b and d. Nonetheless, our main result is that for finite-time driving speeds the station is different and one may have $\Delta Q > 0$, thus $\eta > \eta^*$. The interesting observation is a peak in η at some specific time scale of driving. In the next part we discuss this advantageous in the performance of the engine in more detail.

4.2. Performance of the cycle with real-time endpoints

We first consider the situation in which the speed of compression and expansion processes are identical, i.e. $\tau_{ab} = \tau_{cd}$, which corresponds to the situations shown in the panels (b)–(d) of figure 3. Efficiency of the cycle is plotted as a function of $\tau_{ab,cd}$ using the solid curves in the upper panel of figure 5. We have plotted the efficiency calculated using both the effective Hamiltonian $\hat{H}_{\text{eff}}$ (thick green curves) and the bare Hamiltonian $\hat{H}_S$ (thin green curves). The most striking observation is a peak in the efficiency at some values of $\tau_{ab(cd)}$ which exceeds the efficiency of the quasistatic cycle shown by the dotted black line. To realize the relation between the observed efficiency enhancement and different physical time scales involved in the dynamics of the WS, to say relaxation time τ_R, bath correlation time τ_C, and bath resonance time scale τ_B, we have plotted the efficiency for four different cases. These are considering two different values of the relaxation time, $\tau_R(g_1)$ and $\tau_R(g_2) = \tau_R(g_1)/2$, and two different values of the bath correlation time, $\tau_C(f = 2)$ and $\tau_C(f = 3) = 1.43 \times \tau_C(f = 2)$. Moreover, we set the value of τ_B fixed for all the four mentioned cases. Looking at figure 5, it is clear that the relevant parameter for the observed peak in the efficiency is the bath resonance time τ_B, such that when $\tau_{ab(cd)}$ are close to τ_B we observe the enhancement in the efficiency. On the contrary, it is clear that when the time scale of the drive is close to the bath correlation time τ_C the efficiency decreases. The output power of the cycle for the same settings is also plotted as a function of $\tau_{ab,cd}$ in the lower panel of figure 5. We note that since we are interested in the work done by the external drive, on which one has control, the output power is only plotted with respect to the bare Hamiltonian. Nonetheless, we notice that the difference between the power calculated using the effective Hamiltonian and the bare Hamiltonian was too small to be plotted together here. Interestingly, the average output power benefits from enhancement when $\tau_{ab,cd} \simeq \tau_B$ as well. However, the peak in the power is happening at a slightly larger time scale than those for the efficiency. As expected, the output power decreases by increasing $\tau_{ab,cd}$. The same behavior also holds for very short time scales, when the extractable work diminishes at ultra-fast driving due to an increase in the irreversibility.

Studying the energy flow from or into the WS is essential to comprehend the observed boost in efficiency and power. Without loss of generality, we present the energetic results only for the case with $f = 2$ and $(g_c, g_h) = g_1$. The average heat transferred, average work and the net average work are plotted in figure 6 considering the effective Hamiltonian $\hat{H}_{\text{eff}}$ in the left panel, and the bare Hamiltonian $\hat{H}_S$ in the right panel. Using the effective Hamiltonian to calculate the energy terms leads to some non-zero amount of average work for the isochoric strokes due to the time-dependent Lamb shifts. The corresponding terms are absent when we use the bare Hamiltonian as the drive is off during the isochoric strokes. Moreover, the average work in the expansion stroke is higher when we consider the effective Hamiltonian, which shows up also in the net extractable average work and consequently results into a higher efficiency in comparison to

Figure 8. The net average work and the net heat transferred into the WS as a function of $\tau_{ab,cd}$. The solid green curves correspond to the symmetric case with $\tau_{ab} = \tau_{cd}$, the large dashed red represents the asymmetric case (a), and the small dashed blue to the asymmetric case (b) discussed in the main text. Here we set $f = 2$ and $(g_c, g_h) = g_1$.

the case of using the bare Hamiltonian (see figure 5). This behavior is again due to the non-zero Lamb shift terms and the fact that by including them the effective frequency span of the WS is higher than the bare frequency span $\Delta\omega = \omega_2 - \omega_1$, specifically for $c \to d$ process. The average network approaches to its maximum value corresponding to a quasistatic cycle as we increase $\tau_{ab,cd}$ and decreases by speeding up the drive. One can see that the average heat transferred during the compression and expansion processes goes to zero as we decrease $\tau_{ab,cd}$, because the WS does not have enough time to exchange energy with the baths. Moreover, the heat transferred during the isochoric strokes reaches its non-zero minimum by approaching the diabatic limit (points $\bar{b}$ and $\bar{d}$ in figure 3).

Besides these asymptotic scenarios, we observe a dip in the heat transferred and the net average work at some values of $\tau_{ab,cd}$ coinciding with the peak in the efficiency. The dip especially indicates some extent of suppression of heat transferred to the cold bath. With a given amount of heat absorbed from the hot bath, if the WS dissipates less to the cold bath it means that the work done is higher and thereby the efficiency as well. This may suggest that a faster $a \to b'$ process in figure 3 is in general beneficial, as the state at the endpoint b' gets closer to the equilibrium state at the point c and there would be less dissipated heat to the cold bath. However, the faster the $a \to b'$ process, the less amount of heat is absorbed from the hot bath, which restricts the amount of extractable work too. Note that a similar situation also happens for the $c \to d'$ process considering the heat dissipated during the expansion and the heat absorbed during the thermalization $d' \to a$. Therefore, there must be some trade-off giving us the optimum efficiency in the intermediate situation.

To shed some light on the points discussed above, we consider the distance between the states at some endpoints in figure 3. First, the distance between real-time endpoints $b'(d')$ and fixed equilibrium endpoints $b(d)$ allows us to quantify how far we are from the equilibrium at the end of the compression and expansion processes. Second, the distance between the states at $b'(d')$ and $c(d)$ indicates how far the WS is from the thermal states at the endpoints of the isochoric strokes. To measure the distance between two states ρ_1 and ρ_2 we use the relative entropy between them defined by

$$S(\hat{\rho}_1 \| \hat{\rho}_2) = \text{tr}[\hat{\rho}_1 \log(\hat{\rho}_1)] - \text{tr}[\hat{\rho}_1 \log(\hat{\rho}_2)]. \tag{27}$$

Looking at the left panel of figure 7, the distance between the endpoint state $\hat{\rho}_{b'(d')}$ and the equilibrium states $\hat{\rho}_{b(d)}$ decreases as we increase the driving duration. An observation in the left panel of this figure is that the two curves cross (the distance between b' and c is equal to the distance between d' and d) when duration of the processes is around τ_C. Note that this coincides with the local minimum in the curve of efficiency. Looking at the right panel of figure 7, we realize the existence of a dip at $\tau_{ab,cd} \simeq \tau_B$ that coincides with the peak in the efficiency.

Now we consider the asymmetric driving scenario where the speeds of compression and expansion differ. In particular we assume two different situations: (a) setting $\tau_{ab} = \tau_D$ fixed while changing τ_{cd} and

(b) setting $\tau_{cd} = \tau_\mathrm{D}$ fixed while varying τ_{ab}. The efficiency and the average output power of these cases are plotted in figure 5 using large dashing red and small dashing blue lines, respectively. Again the thick curves correspond to calculating the energies w.r.t. the effective Hamiltonian and the thin curves to the bare Hamiltonian. Interestingly, efficiency of the asymmetric cycles is always higher than the symmetric ones. However, superiority of the two asymmetric cases with respect to each other depends non-trivially on the time scale of the driving. Let us also examine the energetic of the asymmetric cycles in comparison to the symmetric ones depicted in figure 8. We note that the amount of network is dependent on the total time of the expansion and compression process, $\tau_\mathrm{tot} = \tau_{ab} + \tau_{cd}$, and in general decreases by decreasing τ_tot due to irreversibility. However, within the two asymmetric cycles with the same value of τ_tot, we notice slightly different values for the net average work, indicating again the importance of the finite-time effects in the performance of the heat engines.

5. Conclusions

In conclusion, we have studied the performances of a Stirling cycle when operated as a finite-time quantum heat engine. We first derived a non-Markovian master equation which allows us to study the dynamics of an open quantum system without making any distinction between the time scales of the system and of the environments. Thanks to this, we have been able to study the effect of the competing time scales, such as the typical time scale of the drive and the bath correlation/resonance time, on the performances of the heat engine. The main motivation of this work was to explore the role of the deviation of the real-time endpoints of the compression/expansion processes from the conventional fixed equilibrium endpoints in the performance of the engine. We found that enforcing the WS to come back to the equilibrium states (having conventional isotherms) results in the common intuition that efficiency decreases by speeding up the processes. However, skipping thermalization with the baths and instead following the real-time trajectories of the WS may lead to a higher efficiency. Interestingly, we found that driving the WS at a time scale comparable to the resonance time of the bath, in addition to a boost in the output power, let us get an efficiency that is higher than the efficiency of the quasistatic cycle. One should note, however, that the net extractable work decreases by speeding up the cycle due to higher degree of irreversibility. The other important finding in this work was the non-trivial dependency of the performance of the heat engine on the individual speed of the compression and expansion processes. Interestingly, one may achieve better performances by applying asymmetric compression and expansion speeds rather than a symmetric one. The latter opens new possibilities to optimize the performance of the quantum heat engines. As an outlook of our work, it would important to explore how finite-time effects influence the operating range and performance of the quantum Stirling cycle working as a refrigerator. In addition, our results motivate for further studies aiming at optimization of quantum thermodynamic cycles with finite-time driving protocols, especially from an application point of view. We stress that in an experimental implementation of the thermodynamic cycles it might be quite likely to miss the isothermal constraint (having equilibrium state at the end of the compression/expansion process), so analyzing the performance of the cycle with a real-time dynamical point of view, as we did in the current work, proves necessary.

Data availability statement

All data that support the findings of this study are included within the article (and any supplementary files).

Appendix A. Master equation

A.1. Calculating the transition rates
Here we briefly elaborate our approach to calculate the transition rates of the master equation

$$\mathcal{L}_t[\hat{\rho}(t)] = -i[\hat{H}_S(t), \hat{\rho}(t)] + \int_0^t d\tau \Phi(t-\tau)[\hat{\tilde{S}}(t,\tau)\hat{\rho}(t), \hat{S}(t)] + \text{h.c.} \; . \tag{A.1}$$

The unitary propagator $\hat{U}(t,0) = T \exp\left(-i\int_0^t d\tau \, \hat{H}_S(\tau)\right)$ can be calculated numerically in a time interval $[0, t_{\max}]$ by solving the Schrödinger equation

$$\frac{d}{dt}\hat{U}(t,0) = -i\hat{H}_S(t)\hat{U}(t,0). \tag{A.2}$$

Then owing to the divisibility of the unitary propagator we get

$$\hat{U}(t,\tau) = \hat{U}(t,0)\hat{U}(\tau,0)^\dagger, \quad 0 \leqslant \tau < t \leqslant t_{\max} \tag{A.3}$$

Inserting this solution in $\hat{\tilde{S}}(t,\tau) = \hat{U}(t,\tau)\hat{S}(\tau)\hat{U}(t,\tau)^\dagger$ and decomposing the operators with respect to Pauli operator basis $\{\hat{\sigma}_0 = \hat{I}, \; \hat{\sigma}_x, \; \hat{\sigma}_y, \; \hat{\sigma}_z\}$ we get

$$\hat{\tilde{S}}(t,\tau) = \sum_i \tilde{s}_i(t,\tau)\hat{\sigma}_i. \tag{A.4}$$

By introducing a similar decomposition for the operator $\hat{S}(t)$ given by $\hat{S}(t) = \Sigma_j \zeta_j(t)\hat{\sigma}_j$, the second term on the rhs of equation (A.1) will be rewritten as

$$\sum_{i,j} R_{ij}(t)[\hat{\sigma}_i\hat{\rho}(t), \hat{\sigma}_j] + \text{h.c.}, \tag{A.5}$$

with the time-dependent rates

$$R_{ij}(t) = \zeta_j(t)\int_0^t d\tau \Phi(t-\tau)\tilde{s}_i(t,\tau). \tag{A.6}$$

A.2. ME decomposed with respect to the instantaneous energy basis of the open quantum system

Consider an instantaneous eigenvector of $\hat{H}_S(t)$ denoted by $|\epsilon_i(t)\rangle$ corresponding to the instantaneous energy eigenvalue $\epsilon_i(t)$. By defining $\hat{E}_{nm}(t) = |\epsilon_n(t)\rangle \langle\epsilon_m(t)|$, one can decompose $\hat{S}$ and $\hat{\tilde{S}}$ as

$$\hat{\tilde{S}}(t,\tau) = \sum_{n,m} \tilde{\xi}_{nm}(t,\tau)\hat{E}_{nm}(t), \tag{A.7}$$

$$\hat{S}(t) = \sum_{n,m} \eta_{nm}(t)\hat{E}_{nm}(t). \tag{A.8}$$

By inserting these expressions in equation (A.1), the second term on the rhs takes a form given by

$$\sum_{n,m}\sum_{r,s} \left\{ R_{nm,rs}^{(\downarrow)}(t) \left[\hat{E}_{nm}(t)\hat{\rho}(t)\hat{E}_{rs}(t) - \hat{E}_{rs}(t)\hat{E}_{nm}(t)\hat{\rho}(t)\right] \right.$$
$$\left. + R_{nm,rs}^{(\uparrow)}(t) \left[\hat{E}_{rs}(t)\hat{\rho}(t)\hat{E}_{nm}(t) - \hat{\rho}(t)\hat{E}_{nm}(t)\hat{E}_{rs}(t)\right] \right\}, \tag{A.9}$$

with

$$R_{nm,rs}^{(\downarrow)}(t) = \int_0^t d\tau \Phi(t-\tau)\tilde{\xi}_{nm}(t,\tau)\eta_{nm}(t), \tag{A.10}$$

$$R_{nm,rs}^{(\uparrow)}(t) = \int_0^t d\tau \Phi(t-\tau)^* \tilde{\xi}_{nm}(t,\tau)\eta_{nm}(t). \tag{A.11}$$

One can further arrange equation (A.9) into rotating (R) and counter-rotating (CR) parts with respect to the instantaneous energy basis. The rotating part takes the form

$$\mathcal{L}_t^{(R)}[\hat{\rho}(t)] = \sum_{n\neq m} \left\{ R_{nm,mn}^{(\downarrow)}(t) \left[\hat{E}_{nm}(t)\hat{\rho}(t)\hat{E}_{mn}(t) - \hat{E}_{mn}(t)\hat{E}_{nm}(t)\hat{\rho}(t)\right] \right.$$
$$\left. + R_{nm,mn}^{(\uparrow)}(t) \left[\hat{E}_{mn}(t)\hat{\rho}(t)\hat{E}_{nm}(t) - \hat{\rho}(t)\hat{E}_{nm}(t)\hat{E}_{mn}(t)\right] \right\}, \tag{A.12}$$

while the counter-rotating part $\mathcal{L}_t^{(CR)}$ includes all the remaining terms.

We focus now on the specific model considered in this paper given by the Hamiltonian in equation (8), and instantaneous cycle energy basis labeled by $|\epsilon_e(t)\rangle$ and $|\epsilon_g(t)\rangle$. Having $\hat{S}(t) = \lambda(t)\hat{\sigma}_y$, and the expression for the energy basis given in equations (10) and (11), we get

$$\hat{S}(t) = \lambda(t)\left(-i\hat{E}_{eg}(t) + i\hat{E}_{ge}(t)\right). \tag{A.13}$$

Considering the numerical solution in equation (A.4), a decomposition for $\hat{\tilde{S}} = \sum_{n,m=e,g}\tilde{s}_{nm}(t,\tau)\hat{E}_{nm}(t)$ in the energy basis is given by

$$
\hat{\tilde{S}}(t,\tau) = \left(\tilde{s}_0 + \frac{\tilde{s}_x\Delta + \tilde{s}_z q(t)}{\sqrt{q(t)^2 + \Delta^2}}\right)\hat{E}_{ee}(t) + \left(\tilde{s}_0 - \frac{\tilde{s}_x\Delta + \tilde{s}_z q(t)}{\sqrt{q(t)^2 + \Delta^2}}\right)\hat{E}_{gg}(t)
$$
$$
+ \left(-i\tilde{s}_y + \frac{\tilde{s}_x q(t) - \tilde{s}_z\Delta}{\sqrt{q(t)^2 + \Delta^2}}\right)\hat{E}_{eg}(t) + \left(i\tilde{s}_y + \frac{\tilde{s}_x q(t) - \tilde{s}_z\Delta}{\sqrt{q(t)^2 + \Delta^2}}\right)\hat{E}_{ge}(t), \tag{A.14}
$$

where $\tilde{s}_i \equiv \tilde{s}_i(t,\tau)$. Note that one has $R^{(\downarrow)}_{eg,ge}(t) = R^{(\uparrow)}_{ge,eg}(t)^*$ and $R^{(\downarrow)}_{ge,eg}(t) = R^{(\uparrow)}_{eg,ge}(t)^*$. Moreover, since $\tilde{s}_0(t,\tau) \equiv 0$ and all other $\tilde{s}_i$ are real valued, we also have $R^{(\downarrow)}_{ee,ge}(t) = -R^{(\downarrow)}_{gg,eg}(t)^*$ and $R^{(\uparrow)}_{ee,eg}(t) = -R^{(\uparrow)}_{gg,ge}(t)^*$. Accordingly, the rotating part $\mathcal{L}^{(R)}_t$ reads

$$
\mathcal{L}^{(R)}_t[\hat{\rho}(t)] = -i\left[\delta^{(R)}_L(t)\hat{H}_S(t), \hat{\rho}(t)\right]
$$
$$
+ \gamma^{(\downarrow)}(t)\left[\hat{L}(t)\hat{\rho}(t)\hat{L}^\dagger(t) - \frac{1}{2}\{\hat{L}^\dagger(t)\hat{L}(t), \hat{\rho}(t)\}\right]
$$
$$
+ \gamma^{(\uparrow)}(t)\left[\hat{L}^\dagger(t)\hat{\rho}(t)\hat{L}(t) - \frac{1}{2}\{\hat{L}(t)\hat{L}^\dagger(t), \hat{\rho}(t)\}\right], \tag{A.15}
$$

where $\hat{L}(t) = \hat{E}_{ge}(t)$. The explicit expressions for the rates are $\gamma^{(\downarrow)}(t) = 2\mathrm{Re}[R^{(\downarrow)}_{ge,eg}(t)]$, $\gamma^{(\uparrow)}(t) = 2\mathrm{Re}[R^{(\uparrow)}_{ge,eg}(t)^*]$, and $\delta^{(R)}_L(t) = (\mathrm{Im}[R^{(\downarrow)}_{ge,eg}(t)] + \mathrm{Im}[R^{(\uparrow)}_{ge,eg}(t)^*])/2$. In addition the counter-rotating Lamb shift is given by $\delta^{(CR)}_L(t) = \mathrm{Im}[R^{(\downarrow)}_{ee,eg}(t)]$. However, the expression for the counter-rotating dissipator is so lengthy that does not fit here.

Appendix B. A possible implementation using superconducting circuits

We specifically consider a setup implementable with a superconducting circuit schematically shown in figure B1. It is worth mentioning that a related design has been also put forward in references [46, 60]. In order to realize the connection and disconnection from the baths required at steps *b* and *d* in the cycle, a tunable coupling element between the TLS and the resistor is required. Several types of tunable couplers have been proposed and studied, e.g. based on dressed states [61], additional qubits [62], additional single Josephson junctions with current bias [63]. Here we propose using a SQUID junction whose effective inductance is modulated by a bias magnetic field [64, 65]. However, for the sake of simplicity, we assume an ideal connection/disconnection protocol described by a piece-wise continuous function $\lambda_\alpha(t)$, as shown in the panel (d) of figure 1. According to this setup, the resonance frequency of the baths resonators are given by $\omega_i = 1/\sqrt{L_i C_i}$, and their quality factors by $f_i = R_i^{-1}\sqrt{L_i/C_i}$.

Appendix C. Analytic considerations for the asymptotic Stirling cycles

Apart from the dynamical approach of the paper, we provide some analytic analysis of the energy transferred for some asymptotic cases. Assume that at the end of the isochoric strokes $b \to c$ and $d \to a$ the TLS relaxes to the corresponding thermal states
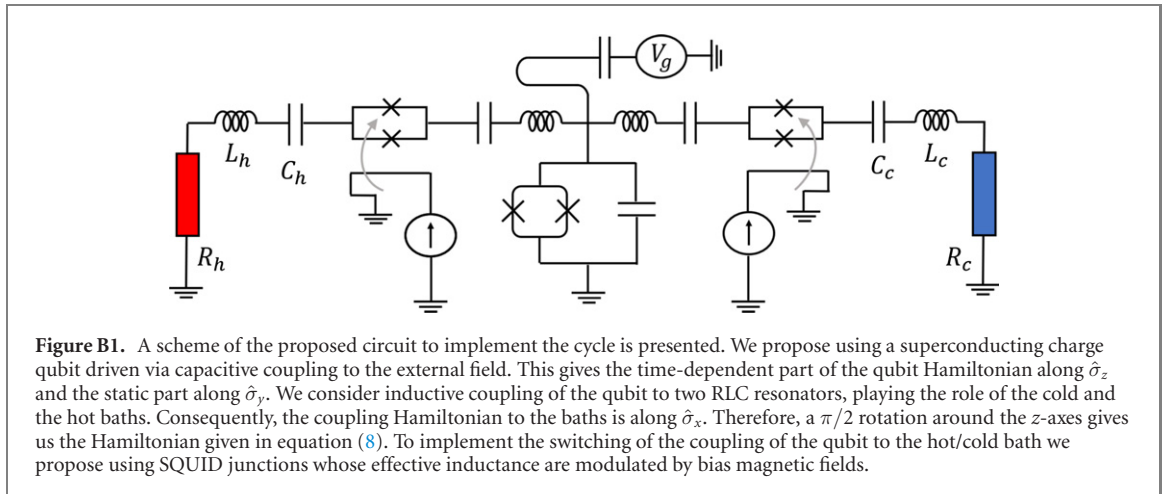
$$\hat{\rho}_c = \frac{e^{-\beta_c\hat{H}_S(t_c)}}{\mathrm{tr}[e^{-\beta_c\hat{H}_S(t_c)}]}, \qquad \hat{\rho}_a = \frac{e^{-\beta_h\hat{H}_S(t_a)}}{\mathrm{tr}[e^{-\beta_h\hat{H}_S(t_a)}]}. \tag{C.1}$$

With this assumption and by considering the bare Hamiltonian of the TLS, one can analyze the energetic of the quantum Stirling cycle with regards to the four asymptotic cases listed below.

C.1. The (ss) cycle: ideally slow compression and slow expansion
In this extreme, both the compression and the expansion processes are ideally slow, i.e. the qubit follows a trajectory on which it is always at thermal equilibrium with the bath. The heat transfer during the four

Figure B1. A scheme of the proposed circuit to implement the cycle is presented. We propose using a superconducting charge qubit driven via capacitive coupling to the external field. This gives the time-dependent part of the qubit Hamiltonian along $\hat{\sigma}_z$ and the static part along $\hat{\sigma}_y$. We consider inductive coupling of the qubit to two RLC resonators, playing the role of the cold and the hot baths. Consequently, the coupling Hamiltonian to the baths is along $\hat{\sigma}_x$. Therefore, a $\pi/2$ rotation around the z-axes gives us the Hamiltonian given in equation (8). To implement the switching of the coupling of the qubit to the hot/cold bath we propose using SQUID junctions whose effective inductance are modulated by bias magnetic fields.

strokes then is calculated by [54]($\hbar = 1$, $k_{\rm B} = 1$)

$$\langle Q_{ab} \rangle = \beta_{\rm h}^{-1} \int_a^b {\rm d}S = \beta_{\rm h}^{-1}[S(\hat{\rho}_{t_b}) - S(\hat{\rho}_{t_a})], \tag{C.2}$$

$$\langle Q_{bc} \rangle = {\rm Tr}[\hat{H}_{\rm S}(t_c)\hat{\rho}_{t_c}] - {\rm Tr}[\hat{H}_{\rm S}(t_b)\hat{\rho}_{t_b}], \tag{C.3}$$

$$\langle Q_{cd} \rangle = \beta_{\rm c}^{-1} \int_c^d {\rm d}S = \beta_{\rm c}^{-1}[S(\hat{\rho}_{t_d}) - S(\hat{\rho}_{t_c})], \tag{C.4}$$

$$\langle Q_{da} \rangle = {\rm Tr}[\hat{H}_{\rm S}(t_d)\hat{\rho}_{t_d}] - {\rm Tr}[\hat{H}_{\rm S}(t_a)\hat{\rho}_{t_a}], \tag{C.5}$$

where $S(\hat{\rho})$ is the von Neumann entropy of a given state $\hat{\rho}$. For a TLS with the level populations ρ_{ee} and ρ_{gg} one has

$$S(\hat{\rho}) = -(\rho_{ee} \log[\rho_{ee}] + \rho_{gg} \log[\rho_{gg}]). \tag{C.6}$$

Then according to the first law of thermodynamics we get the net average work done on the qubit by $\langle W \rangle_{\rm net} = -(\langle Q_{ab} \rangle + \langle Q_{bc} \rangle + \langle Q_{cd} \rangle + \langle Q_{da} \rangle)$.

C.2. The (fs) cycle: ideally fast compression and slow expansion

In this extreme, $a \rightarrow b$ process is done in a finite but very fast time scale, such that the process is diabatic. For a sufficiency fast process, TLS does not have time to exchange heat with the hot bath and $\langle Q_{ab} \rangle = 0$. Nonetheless, there is some non-zero average work done on the TLS that can be obtained by the change in its internal energy. Since the process is diabatic, state of the TLS remains at its initial configuration at time t_a, therefore

$$\langle W_{ab} \rangle = {\rm tr}\left[(\hat{H}_{\rm S}(t_b) - \hat{H}_{\rm S}(t_a))\hat{\rho}_{t_a}\right]. \tag{C.7}$$

The remaining energy terms can be calculated similar to the (ss) case.

C.3. The (sf) cycle: ideally slow compression and fast expansion

This is the opposite situation of the (fs) cycle, such that $\langle Q_{cd} \rangle = 0$ and

$$\langle W_{cd} \rangle = {\rm tr}\left[(\hat{H}_{\rm S}(t_d) - \hat{H}_{\rm S}(t_c))\hat{\rho}_{t_c}\right]. \tag{C.8}$$

C.4. The (ff) cycle: ideally fast compression and fast expansion

Finally when both the processes are diabatic, one has $\langle Q_{ab} \rangle = \langle Q_{cd} \rangle = 0$ and the amounts of average work can be obtained as discuss in the two previous cases.

ORCID iDs

S Hamedani Raja ⬤ https://orcid.org/0000-0002-7881-1247
G S Paraoanu ⬤ https://orcid.org/0000-0003-0057-7275
N Lo Gullo ⬤ https://orcid.org/0000-0002-8178-9570

References

[1] Binder F, Correa L A, Gogolin C, Anders J and Adesso G (ed) 2018 *Thermodynamics in the Quantum Regime* (Berlin: Springer)
[2] Vinjanampathy S and Anders J 2016 *Contemp. Phys.* **57** 545–79
[3] Goold J, Huber M, Riera A, Rio L d and Skrzypczyk P 2016 *J. Phys. A: Math. Theor.* **49** 143001
[4] Silveri M P, Tuorila J A, Thuneberg E V and Paraoanu G S 2017 *Rep. Prog. Phys.* **80** 056002
[5] Alicki R 1979 *J. Phys. A: Math. Gen.* **12** L103–7
[6] Scully M O, Zubairy M S, Agarwal G S and Walther H 2003 *Science* **299** 862–4
[7] Niskanen A O, Nakamura Y and Pekola J P 2007 *Phys. Rev.* B **76** 174523
[8] Quan H T, Liu Y x, Sun C P and Nori F 2007 *Phys. Rev.* E **76** 031105
[9] Gelbwaser-Klimovsky D, Alicki R and Kurizki G 2013 *Phys. Rev.* E **87** 012140
[10] Kosloff R and Levy A 2014 *Annu. Rev. Phys. Chem.* **65** 365–93
[11] Alicki R and Gelbwaser-Klimovsky D 2015 *New J. Phys.* **17** 115012
[12] Campisi M and Fazio R 2016 *Nat. Commun.* **7** 11895
[13] Karimi B and Pekola J P 2016 *Phys. Rev.* B **94** 184503
[14] Roßnagel J, Dawkins S T, Tolazzi K N, Abah O, Lutz E, Schmidt-Kaler F and Singer K 2016 *Science* **352** 325–9
[15] Tan K Y, Partanen M, Lake R E, Govenius J, Masuda S and Möttönen M 2017 *Nat. Commun.* **8** 15189
[16] Kosloff R and Rezek Y 2017 *Entropy* **19** 136
[17] Roßnagel J, Abah O, Schmidt-Kaler F, Singer K and Lutz E 2014 *Phys. Rev. Lett.* **112** 030602
[18] Uzdin R, Levy A and Kosloff R 2015 *Phys. Rev.* X **5** 031044
[19] Jaramillo J, Beau M and Campo A d 2016 *New J. Phys.* **18** 075019
[20] Klaers J, Faelt S, Imamoglu A and Togan E 2017 *Phys. Rev.* X **7** 031044
[21] Deffner S 2018 *Entropy* **20** 875
[22] Klatzow J *et al* 2019 *Phys. Rev. Lett.* **122** 110601
[23] Mukherjee V, Kofman A G and Kurizki G 2020 *Commun. Phys.* **3** 8
[24] Feldmann T and Kosloff R 2000 *Phys. Rev.* E **61** 4774–90
[25] Kosloff R and Feldmann T 2002 *Phys. Rev.* E **65** 055102
[26] Feldmann T and Kosloff R 2003 *Phys. Rev.* E **68** 016101
[27] Plastina F, Alecce A, Apollaro T J G, Falcone G, Francica G, Galve F, Lo Gullo N and Zambrini R 2014 *Phys. Rev. Lett.* **113** 260601
[28] Alecce A, Galve F, Gullo N L, Dell'Anna L, Plastina F and Zambrini R 2015 *New J. Phys.* **17** 075007
[29] Brandner K, Bauer M and Seifert U 2017 *Phys. Rev. Lett.* **119** 170602
[30] Pekola J P, Karimi B, Thomas G and Averin D V 2019 *Phys. Rev.* B **100** 085405
[31] Ghosh A, Mukherjee V, Niedenzu W and Kurizki G 2019 *Eur. Phys. J. Spec. Top.* **227** 2043–51
[32] Marcantoni S, Alipour S, Benatti F, Floreanini R and Rezakhani A T 2017 *Sci. Rep.* **7** 12447
[33] Mukherjee V, Giovannetti V, Fazio R, Huelga S F, Calarco T and Montangero S 2015 *New J. Phys.* **17** 063031
[34] Das A and Mukherjee V 2020 *Phys. Rev. Res.* **2** 033083
[35] Curzon F L and Ahlborn B 1975 *Am. J. Phys.* **43** 22–4
[36] Esposito M, Kawai R, Lindenberg K and Van den Broeck C 2010 *Phys. Rev. Lett.* **105** 150603
[37] Ma Y H, Xu D, Dong H and Sun C P 2018 *Phys. Rev.* E **98** 042112
[38] Abiuso P and Perarnau-Llobet M 2020 *Phys. Rev. Lett.* **124** 110606
[39] Abiuso P, Miller H J D, Perarnau-Llobet M and Scandi M 2020 *Entropy* **22** 1076
[40] Brandner K and Saito K 2020 *Phys. Rev. Lett.* **124** 040602
[41] Torrontegui E, Ibáñez S, Martínez-Garaot S, Modugno M, del Campo A, Guéry-Odelin D, Ruschhaupt A, Chen X and Muga J G 2013 *Shortcuts to Adiabaticity Advances in Atomic, Molecular, and Optical Physics* (*Advances in Atomic, Molecular, and Optical Physics* vol 62) ed E Arimondo, P R Berman and C C Lin (New York: Academic) ch 2 pp 117–69
[42] Guéry-Odelin D, Ruschhaupt A, Kiely A, Torrontegui E, Martínez-Garaot S and Muga J G 2019 *Rev. Mod. Phys.* **91** 045001
[43] Vepsäläinen A, Danilin S and Paraoanu G S 2019 *Sci. Adv.* **5** eaau5999
[44] Vepsäläinen A and Paraoanu G S 2020 *Adv. Quantum Tech.* **3** 1900121
[45] Alipour S, Chenu A, Rezakhani A T and del Campo A 2020 *Quantum* **4** 336
[46] Funo K, Lambert N, Karimi B, Pekola J P, Masuyama Y and Nori F 2019 *Phys. Rev.* B **100** 035407
[47] Abah O and Paternostro M 2019 *Phys. Rev.* E **99** 022110
[48] Vacanti G, Fazio R, Montangero S, Palma G M, Paternostro M and Vedral V 2014 *New J. Phys.* **16** 053017
[49] Suri N, Binder F C, Muralidharan B and Vinjanampathy S 2018 *Eur. Phys. J. Spec. Top.* **227** 203–16
[50] Scandi M and Perarnau-Llobet M 2019 *Quantum* **3** 197
[51] Dann R, Levy A and Kosloff R 2018 *Phys. Rev.* A **98** 052129
[52] Dann R, Tobalina A and Kosloff R 2019 *Phys. Rev. Lett.* **122** 250402
[53] Pancotti N, Scandi M, Mitchison M T and Perarnau-Llobet M 2020 *Phys. Rev.* X **10** 031015
[54] Huang X L, Niu X Y, Xiu X M and Yi X X 2014 *Eur. Phys. J.* D **68** 32
[55] Yin Y, Chen L and Wu F 2017 *Eur. Phys. J. Plus* **132** 45
[56] Serafini G, Zippilli S and Marzoli I 2020 Optomechanical stirling heat engine driven by feedback-controlled light *Phys. Rev.* A **102** 053502
[57] Kofman A G and Kurizki G 2004 *Phys. Rev. Lett.* **93** 130406
[58] Gordon G, Erez N and Kurizki G 2007 *J. Phys. B: At. Mol. Opt. Phys.* **40** S75–93
[59] Alipour S, Benatti F, Bakhshinezhad F, Afsary M, Marcantoni S and Rezakhani A T 2016 *Sci. Rep.* **6** 35568
[60] Ronzani A, Karimi B, Senior J, Chang Y-C, Peltonen J T, Chen C and Pekola J P 2018 *Nat. Phys.* **14** 991–5
[61] Paraoanu G S 2006 *Phys. Rev.* B **74** 140504
[62] Niskanen A O, Harrabi K, Yoshihara F, Nakamura Y, Lloyd S and Tsai J S 2007 *Science* **316** 723–6
[63] Blais A, van den Brink A M and Zagoskin A M 2003 *Phys. Rev. Lett.* **90** 127901
[64] Mundada P, Zhang G, Hazard T and Houck A 2019 *Phys. Rev. Appl.* **12** 054023
[65] Chen Y *et al* 2014 *Phys. Rev. Lett.* **113** 220502